

Research Paper

Crank angle-resolved mass flow characterization of engine exhaust pulsations using a Pitot tube and thin-wire thermocouples

Beichuan Hong^{*}, Varun Venkataraman, Mihai Mihaescu, Andreas Cronhjort

KTH Royal Institute of Technology, Brinellvägen 83, Stockholm, 100 44, Sweden

ARTICLE INFO

Keywords:

Unsteady flow
Exhaust pulses
Temporally-resolved measurement
Gas temperature sensitivity

ABSTRACT

Characterizing pulsating flow in high-temperature, high-pressure engine exhaust gas is crucial for the development and optimization of exhaust energy recovery systems. However, the experimental investigation of engine exhaust pulses is challenging due to the difficulties in conducting crank angle-resolved measurements under these unsteady flow conditions. This study contributes to characterizing mass flow pulses from an isolated cylinder exhaust of a heavy-duty diesel engine using a single-pipe measurement system, developed for pulsating flow measurement. A Pitot tube-based approach is adopted to measure exhaust mass flow pulsations, complemented by fast temperature measurements obtained using customized unsheathed thin-wire thermocouples. The on-engine experiment is performed by isolating the in-cylinder trapped mass and the valve opening speed to produce different exhaust pulse waveforms. The adopted approach's sensitivity in resolving instantaneous mass flows is evaluated analytically and experimentally, considering attenuated temperature measurement effects. Based on exhaust flow measurements, mass flow pulses are analyzed with regard to blow-down and scavenge phases. Under the load sweep, the main waveform change occurs during the blow-down phase, with pulse magnitude increasing with the load. In contrast, as the engine speeds up with a comparable trapped mass, the exhaust mass distribution in the blow-down phase decreases from 75.5% at 700 rpm to 41.9% at 1900 rpm. Additionally, it is observed that cycle-to-cycle variations in mass flow pulses align with combustion stability during the blow-down phase and are predominantly influenced by gas-exchange processes during the scavenge phase.

1. Introduction

Transport sector in 2022 remains a significant contributor to global CO₂ emissions, accounting for 21.6% of the annual total [1]. To decarbonize transportation, the combination of both mobility electrification and advancements in the use of internal combustion engines (ICEs) with carbon-neutral or carbon-free fuels may be the most practical near-term solution [2]. Technological developments in clean and high-efficiency ICEs are especially sought after for heavy-duty (HD) applications. In these cases, the progression of vehicle electrification faces challenges due to battery energy density and degradation issues [3], as well as the cost of charging infrastructure [4]. Approximately 20%–40% of the fuel energy persists in the burned gas after combustion and is discharged into the ICE exhaust system. Such exhaust loss has been observed in both on-road transport [5] and marine applications [6]. Consequently, energy harvesting technologies through the exhaust systems, such as turbochargers or other waste energy recovery (WER) devices, have been highlighted as a promising approach to further increase engine thermal efficiency and mitigate emissions [7].

1.1. Literature review

1.1.1. Importance of resolving ICE exhaust pulsations

Due to the exhaust valve's cyclic motion, the high-pressure and high-temperature burned gas is discharged from the cylinder into the exhaust system as high-frequency turbulent pulsating flows. Such unsteady exhaust flow conditions significantly affect the performance of the WER processes downstream. For instance, Liu and Copeland [8] measured a transient negative turbine work amounting to approximately 15% of the turbine's net work when subjected to 20 Hz pulsating flows. Mosca and Mihaescu [9] conducted a numerical parametric study on the response of a radial turbine to engine pulsating flows and observed that increasing the pulse amplitude and decreasing the pulse frequency resulted in a decrease in the turbine's isentropic efficiency.

In addition to turbocharger performance, resolving flow parameters in unsteady exhaust conditions can also facilitate the development and optimization of other WER devices. With a high-pressure flow rig

^{*} Corresponding author.

E-mail addresses: beichuan@kth.se (B. Hong), varunve@kth.se (V. Venkataraman), mihai@mech.kth.se (M. Mihaescu), andreas.cronhjort@itm.kth.se (A. Cronhjort).

<https://doi.org/10.1016/j.applthermaleng.2023.121725>

Received 24 May 2023; Received in revised form 28 September 2023; Accepted 1 October 2023

Available online 5 October 2023

1359-4311/© 2023 The Author(s). Published by Elsevier Ltd. This is an open access article under the CC BY license (<http://creativecommons.org/licenses/by/4.0/>).

to produce engine exhaust-like pulses, Simonetti et al. [10] reported that pulsating flows enhance convective heat transfers, indicating more heat loss through pipe walls under unsteady exhaust conditions. Nour Eddine et al. [11] investigated a thermoelectric generator for energy recovery from exhaust pulsations, observing that the pulsating flow primarily accounted for a 30% output power difference compared to a steady flow scenario with identical inlet temperature and mass flow. In particular, Gundmalm et al. [12] designed an exhaust manifold and utilized variable valve timing technology to divide the exhaust event into the high-energy blow-down exhaust phase and the subsequent scavenge exhaust phase, thereby extracting more exhaust power and bypassing pumping loss. In terms of available energy carried by exhaust pulses, based on the crank angle-resolved exhaust flow parameters from simulation, Mahabadipour et al. [13] quantified the difference in exergy rates between the blow-down and scavenge phases. However, it should be noted that most previous studies on exhaust WER devices that used time-varying flow parameters relied on simulation-based approaches. These approaches are dependent on the quality of the model used to predict flow physical properties and are highly limited by the accuracy of the boundary conditions used to represent actual engine operating conditions. Therefore, the necessity for advancing measurement techniques for exhaust pulsating flow parameters remains significant, as such techniques can not only provide direct flow measurement outcomes but also facilitate flow model validation with more precise simulation boundaries.

1.1.2. Commonly used methods for exhaust flow measurement and their limitations

Three fundamental flow parameters, i.e., pressure, temperature, and mass flow (or velocity), are mainly utilized to describe the flow conditions in the ICE context [14]. To capture the time-varying flow parameters of exhaust pulses, several difficulties with regard to measurement techniques still remain. Except for the fast pressure measurement, which implements the piezoresistive sensor as a well-established solution [15], the commercially available flow measurement of the remaining parameters are limited by the sensor response time. In terms of exhaust gas temperature measurement, the high thermal inertia of the conventional mineral insulated metal sheathed (MIMS) thermocouple with typically 3–4.5 mm wire diameter limits the dynamic response. As for mass flow, standard flowmeter techniques commercially available, such as venturi, rotameter, vortex flowmeter, electromagnetic flowmeter, and hot-film, are not suitable for detecting high-amplitude and high-frequency engine pulsating flows, as they are developed for steady flow environments [16]. Moreover, the high temperature range of engine exhaust pulses, particularly in upstream turbine conditions exceeds the operational temperature limits of these conventional flow meters.

1.1.3. Fast measurement of exhaust mass flow pulses

In literature, a few studies have attempted to measure crank angle-based on-engine exhaust mass flow (or velocity). An ultrasound flowmeter has been developed to detect the instantaneous flow velocity and temperature of the engine exhaust [17]. Ehrlich et al. [18] implemented a particle image velocimetry (PIV) to characterize the flow field at a turbine volute inlet. The highly unsteady flow measured by using laser diagnostics indicated a significant departure from the steady flow assumption regarding the flow energy calculation at the turbine inlet. However, the measurement techniques above have not been widely adopted at the test facilities due to their configuration complexity, lack of robustness, and high costs. In a subsequent investigation, Ehrlich [19] compared the differential pressure method (i.e., Pitot tube) to PIV measurements at the turbine inlet and indicated comparable velocity waveforms with maximum absolute deviations of ~10 m/s at low loads. Later, the differential pressure method using a Pitot tube has been applied in the direct measurement of exhaust pulsating flows. For instance, Nakamura et al. [20] reported the nonlinearity between

dynamic pressure from the Pitot tube measurement and exhaust flow rate under the pulsating flow condition at the tailpipe. Based on the instantaneous mass flow from a Pitot tube, Fonseca González et al. [21] calculated and calibrated the averaged exhaust mass flow at the vehicle tailpipe for a portable emission measurement system. In addition, the engine's air-fuel ratio in Fonseca González et al. [21] has been used to determine the molecular weight and density of the exhaust gas for improving the mass flow rate accuracy.

1.2. Research gaps

Although previous studies have addressed the Pitot tube's capability to measure instantaneous exhaust mass, many research gaps still exist regarding the Pitot tube application under pulsating flow conditions. First, the implementation of the Pitot tube is based on the differential pressure method, which involves the gas temperature. As mentioned previously, the fast measurement of exhaust temperature pulsations is highly attenuated by the conventional MIMS thermocouple. To the best of the authors' knowledge, no study has evaluated the effect of attenuated temperature pulsations on the mass flow measurement in the Pitot tube-based approach under engine exhaust conditions. Another research gap is the measuring location, where most previous studies focused on either turbine performance with unsteady inlet flows on-engine or the exhaust flow rates at the tailpipe. Consequently, the exhaust pulses at these measuring locations have primarily been influenced by interactions with exhaust devices (e.g., turbochargers, after-treatment, or waste heat recovery) or pulses emanating from other cylinders. The measurement of a single pulse during the exhaust valve event remains to be investigated. Furthermore, the discussion in literature on exhaust pulses has been mainly simulation-based, while the characterization of exhaust pulsating flows under different engine operating conditions is yet to be experimentally determined.

1.3. Contributions of the present work

This study aims to address the challenges of characterizing pulsating flow in combustion engines by employing a Pitot tube approach to examine the flow from an isolated one-cylinder exhaust of a HD engine operating under varying load and speed conditions. The major contributions of the present work are as follows:

- Implement a Pitot tube-based approach within a single-pipe measurement system to capture the crank angle-resolved mass flow from an isolated one-cylinder exhaust. The single-pipe measurement system, integrated into the exhaust system of the tested HD engine, is specifically developed for measuring pulsating flow.
- Quantify the sensitivity of resolving mass flow to different temperature pulsations, both analytically and experimentally, based on fast temperature measurements from customized unsheathed thin-wire thermocouples.
- Characterize the instantaneous exhaust mass flow pulses concerning the blow-down and scavenge phases. In particular, the pulse waveform, arrival time at the measurement section, mass distribution over exhaust phases, and variation over cycles are further analyzed.

The rest of this paper is organized as follows. Section 2 presents the experimental setup with a special focus on a single-pipe system for measuring exhaust pulsation. The Pitot tube-based approach is introduced to resolve exhaust mass flow pulses. In Section 3, the measurement accuracy is validated and temperature sensitivity of the proposed approach is discussed. Then, the characterization of pulsating mass flow is analyzed based on the measurement results. Section 4 concludes the paper.

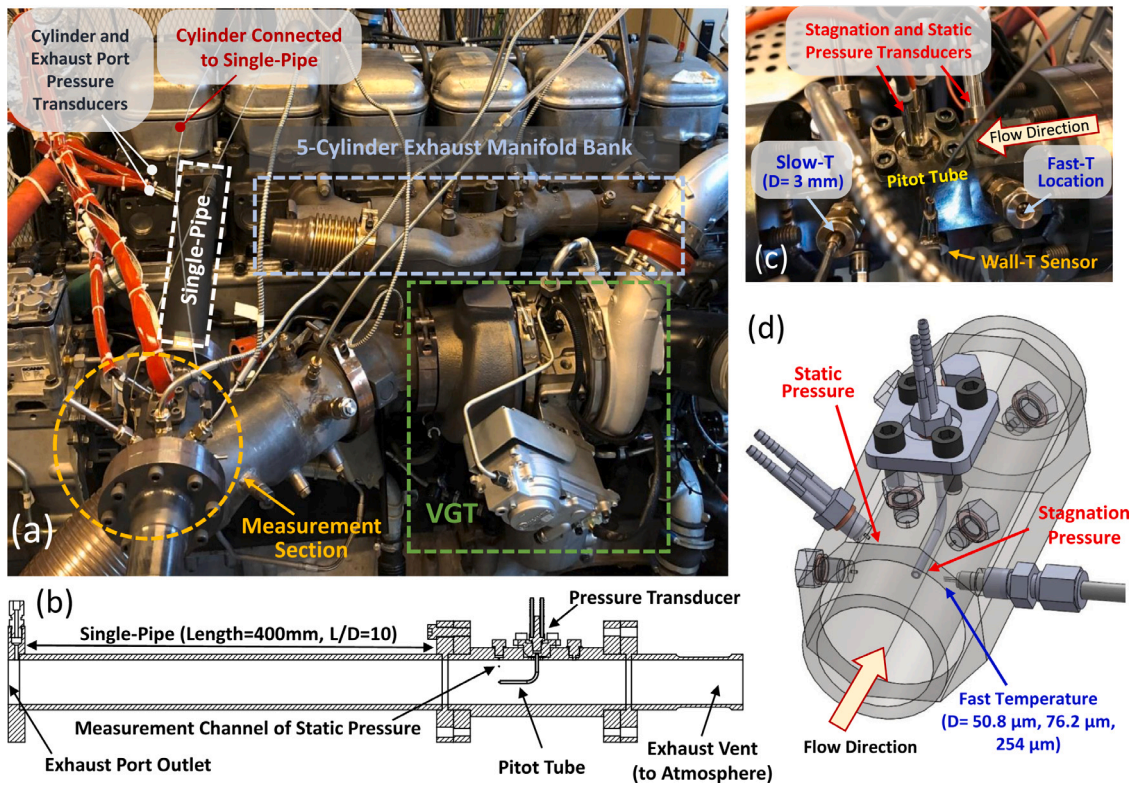


Fig. 1. Schematic of experimental setup and the single-pipe measurement system.

2. Methodology

This study integrates a single-pipe measurement section into an HD engine to measure exhaust pulses. The Pitot tube-based approach for on-engine mass flow pulse measurement is presented in this section. To assess the effect of gas temperature on mass flow measurement, not only fast temperature measurements from different thin wires taken into consideration, but temperature pulsation based on the isentropic relation is also introduced. Moreover, a test matrix is designed with a sweep of engine load and speed, independently varying the in-cylinder trapped mass and valve opening speed.

2.1. Experimental setup

The engine experiment was conducted on a research engine rig at KTH Royal Institute of Technology, Sweden. A Scania D13 6-cylinder HD diesel engine was tested with a single-pipe measurement system developed for measuring the pulsating exhaust flow. The specifications of the tested engine are listed in Table 1. Fig. 1 illustrates the test setup and the single-pipe measurement system. The major change from the default engine configuration in this study was the layout of the exhaust piping, where the single-pipe measurement system was connected to the exhaust port of one cylinder, as shown in Fig. 1a. The outlet of the single-pipe measurement system bypassed the turbocharging stage and was merged into the exhaust vent of the test cell, where the pressure was at the atmospheric level. A variable-geometry turbocharger (VGT) was used to extract the exhaust power of the remaining five cylinders on the turbine side, while its compressor side provided the boost for all six cylinders.

The intention of applying the single-pipe measurement system in this study is to isolate the measurement of a single exhaust pulse from the interaction of other cylinder pulses. A single-pipe with a 400 mm flow development length (see Fig. 1b) was installed to ensure an $L/D \geq 10$ to allow the flow to develop upstream of the measurement section [22]. An octagonal flat face measurement section was used in

the single-pipe measurement system as shown in Fig. 1c. A Pitot tube was mounted on the top of the octagonal measuring section with the tip of the Pitot tube aligning with the pipe centerline. The inner and outer diameters of the Pitot tube were 2 mm and 3 mm, while the horizontal distance between the Pitot tube's tip and stem was ten times more of the outer diameter to avoid the flow boundary layers caused by the Pitot tube stem [15]. A pressure transducer was mounted on the Pitot tube assembly with its cooling system to thermally isolate it from the exhaust temperature. It should be noted that the channel volume from the Pitot tube tip and the pressure transducer location is an acoustic system that may affect the sampling of pressure signals at certain frequencies. To fulfill the measurement purposes, the Pitot tube design must also avoid the interaction between its resonance frequency and the natural frequency of exhaust pulses. More details on the Pitot tube design and its corresponding resonance effect on the stagnation pressure are given in Appendix A.

The static pressure measurement location was assigned on the same plane as the Pitot tube's tip. The pressure transducer was mounted on the wall of the measurement section (see Fig. 1d), assuming that the exhaust pulses were fully developed (i.e., static pressure of pulses is unvarying across the boundary layer) after the entrance length of the single-pipe. Additionally, fast temperature was measured using three customized K-type unsheathed thin-wire thermocouples with wire diameters of 50.8 μm , 76.2 μm , and 254 μm [23]. These customized thin-wire thermocouples used in this study are denoted as T_{f1} , T_{f2} , and T_{f3} , respectively. Furthermore, two bolt-on washer wall thermocouples were mounted on both sides of the measurement section to measure the outer wall temperature, indicating the thermal equilibrium of the measurement section.

The fast pressure measurement utilized Keller M8coolHB piezoresistive pressure transducers with 50 kHz bandwidth for measuring exhaust port outlet pressure, as well as stagnation and static pressures at the measurement section. Cylinder pressure was measured using a Kistler 7061B pressure transducer, while a Keller M5HB pressure transducer was used at the intake manifold for pegging the cylinder

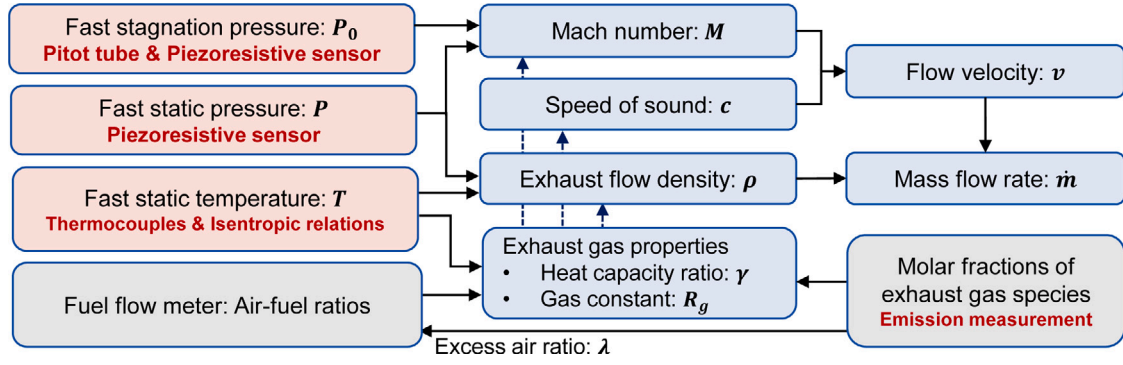


Fig. 2. Flowchart of mass flow measurement using Pitot tube-based approach.

Table 1

Engine specifications.

| | |
|---------------------|-----------------------------------|
| Engine model | Scania D13 |
| Cylinder layout | Inline-6 |
| Bore × Stroke | 130 mm × 160 mm |
| Compression ratio | 18:1 |
| Displacement | 12.7 L |
| Fuel type | Diesel |
| Fuel system | Common rail direct fuel injection |
| IVO/IVC | 346 °CA ATDC/-154 °CA ATDC |
| EVO/EVC | 125 °CA ATDC/ 373 °CA ATDC |
| Turbocharger | VGT Holset |
| Emission compliance | Euro VI |

pressure. Alongside the customized unsheathed thin-wire thermocouples, all fast measurements were simultaneously sampled at 0.1 crank angle resolution over 300 engine cycles using an 8-channel PowerDAQ analog-to-digital converter card. Depending on the engine speed, the sampling frequency of fast measurements ranges from 42 kHz at 700 revolutions per minute (rpm) to 114 kHz at 1900 rpm. Mean pressure and temperature across the gas-exchange system were sampled at 1 Hz using GEMS 3500 series pressure transducers and 3 mm K-type MIMS thermocouples. Gas temperature sensors were calibrated with an Isotech Quick-Cal oven, while pressure transducer calibration sheets were supplied by the manufacturer. Data acquisition for the slow flow measurement was recorded at 1 Hz over 1 min through NuDAM modules and synchronized with engine operation data using an in-house developed code.

The engine test was operated by an AVL Dynodur dynamometer, with a partially open engine control unit (ECU) controlling fuel injection, timing, and VGT rack position. Airflow and fuel mass flow were measured by an annubar flow meter and an AVL 733s fuel consumption meter. A Horiba MEXA 7100 DEGR analyzed the raw emissions from the single-pipe exhaust, which were sampled downstream of the measurement section. The emission readings from the Horiba gas analyzer were averaged over 2 min of measurements with a sampling frequency at 2 Hz. Flow measurements and engine logs were only recorded after achieving thermal equilibrium. Additional information regarding the test setup and sensor calibration for this experimental campaign can be found in Venkataraman et al. [23]. The main specifications of measurement devices and sensors are provided in Table 2.

2.2. Mass flow measurement using pitot tube-based approach

The mass flow measurement using the proposed Pitot tube-based approach is illustrated in Fig. 2. Based on the stagnation-to-static pressure ratio, the Mach number of the compressible flow can be computed using the isentropic relation as

$$\frac{p_0}{p} = \left(1 + \frac{\gamma - 1}{2} M^2\right)^{\frac{\gamma}{\gamma - 1}} \quad (1)$$

where p_0 and p denote stagnation and static pressures. M is the Mach number, and γ is the specific heat ratio. Due to the kinetic energy of the exhaust flow, the stagnation pressure measured in Pitot tube is larger than the static pressure as

$$p_0 = p + \Delta p = p + \frac{1}{2} \rho v^2 \left[1 + \frac{M^2}{4} + \frac{2 - \gamma}{24} M^4 + \dots\right] \quad (2)$$

where Δp is the dynamic pressure caused by flow kinetic energy, and v is the flow velocity. $\rho = p/(R_g T)$ is the flow density, and R_g is the gas constant of exhaust flow. The bracketed terms on the right side of Eq. (2) refers to the compressibility factor which increases with Mach number [24]. The flow velocity can be expressed as

$$v = M c = M \sqrt{\gamma R_g T} \quad (3)$$

where c is the speed of sound. Thus, the mass flow rate can be estimated as

$$\dot{m} = \rho v A \quad (4)$$

where ρv is the mass flux, and A is the cross-sectional area of the measuring section.

In particular, the specific heat ratio can be formulated as a function of gas temperature

$$\gamma(T) = \frac{c_p(T)}{c_p(T) - R_g} \quad (5)$$

$$\frac{c_p(T)}{R_g} = a_1 + a_2 T + a_3 T^2 + a_4 T^3 + a_5 T^4 \quad (6)$$

where c_p is the specific heat at constant pressure. The thermochemical properties of gas mixtures are computed by the ideal gas law and NASA polynomials with coefficients $a_i, i \in [1, 5]$. These gas properties of exhaust flow are determined by the gas composition after the combustion. Based on the air-fuel ratio, the exhaust gas composition after the combustion processes is calculated in Cantera Python library [25] and validated with the emission measurement. The details of gas composition calculation and validation are presented in Appendix B.

2.3. λ -based trapped mass estimation

The modification of the exhaust system might lead to uneven air induction across different cylinders, especially for the single-pipe exhaust without backpressure. To address this issue, the mean exhaust mass flow of the single-pipe was computed using the excess air ratio λ from the Horiba gas analyzer. Horiba gas analyzer employed the “no O₂” method [26] to calculate the excess air ratio from the raw emission measurements. The exhaust mass flow of the single-pipe \dot{m}_{exh} can be estimated as follows:

$$\dot{m}_{exh} = \dot{m}_{air} + \dot{m}_{fuel} \quad (7)$$

$$\lambda = \frac{\dot{m}_{air}}{AFR_{stoich} \dot{m}_{fuel}} \quad (8)$$

Table 2
The main specification of measurement devices and sensors.

| Parameter | Device/Sensor | Range | Accuracy |
|---------------------|---|---|---|
| Slow measurement | | | |
| Gas pressure | GEMS 3500 | 0–6 bar gauge | ±2.5% FS |
| Gas temperature | Pentronic MIMS K-type (D = 3 mm) | ≤ 1200 °C | ±0.1 °C to ±0.4 °C (After calibration) |
| Wall temperature | Bolt-on washer Type-K | ≤ 400 °C | Greater of ±2.5 °C or ±0.75% |
| Fuel mass flow | AVL 733s | 0–150 kg/h | ±0.12% |
| Emission analyzer | Horiba MEXA 7100DEGR | CO: 0–7000 ppm HC, NO _x : 0–5000 ppm CO ₂ : 0%–15% vol. O ₂ : 0%–25% vol. | ±1% FS ±1% FS ±1% FS ±1% FS |
| Fast measurement | | | |
| Cylinder pressure | Kistler 7061 (liquid cooled) | 0–250 bar | ≤ ±0.5% FS |
| Intake pressure | Keller M5HB | 0–10 bar abs. | ±0.1% FS |
| Exhaust pressure | Keller M8coolHB (liquid cooled) | 0–10 bar abs. | ±0.1% FS |
| Exhaust temperature | Customized thin-wires (D = 50.8, 76.2, 254 μm) | | ±0.1 °C to ±0.4 °C (After calibration) |

where \dot{m}_{air} and \dot{m}_{fuel} denote the air mass rates and fuel consumption of the cylinder integrated with the single-pipe system. $AFR_{stoich} = 14.5$ is the stoichiometric air-fuel ratio used in this study for diesel fuel [27]. The value of \dot{m}_{fuel} is taken as the fuel scale measurement scaled down to one cylinder with the assumption of equal fuel distribution among cylinders.

The trapped mass, which represents the in-cylinder gases mass during the closed cycle (i.e., from IVC to EVO), is indicative of the exhaust mass flow rate per cylinder over one engine cycle. The λ -based trapped mass can be determined based on the averaged exhaust mass flow rate:

$$m_{trapped} = \frac{120}{\omega} \dot{m}_{exh} \quad (9)$$

where ω denotes the engine speed, and the factor ‘120’ converts the engine speed unit to cycles per second. This estimation of in-cylinder trapped mass does not consider the blow-by flow into the crankcase. Specifically, this λ -based estimation assumes a consistent presence of residual gas throughout the sampled engine cycles. This is because the trapped mass during one cycle also includes the residual gas left in the cylinder from the previous cycle, whereas the averaged exhaust mass flow rate calculates the trapped mass for the current cycle without accounting for the residual gas. In this study, the trapped mass of the cylinder connected to the single-pipe system is used as a reference to provide comparable engine speed-normalized exhaust mass flow rates.

2.4. Temperature pulsations

In this study, temperature measurements from the unsheathed thin-wire and MIMS thermocouples are interpreted as the static gas temperature of exhaust pulsation. However, it should be noted that gas temperature measurements with invasive sensors (e.g., thermocouples) have several limitations that provide a measurement of the thermocouple junction temperature rather than the static gas temperature. These limitations encompass the dynamic error induced by the thermal inertia of the thermocouple junction, along with conduction and radiation heat losses, which depend on the heat balance within a thermocouple [28]. Additionally, due to the invasive nature, the thermocouples’ measurement represents the recovery temperature, which is at an intermediate level between the static and stagnation temperatures [29]. These limitations inherent in fast temperature measurement necessitate an assessment of how temperature variations impact mass flow measurement.

To evaluate the effect of attenuated temperature measurement on the mass flow measurement, besides three thin-wire thermocouples (i.e., T_{f1} , T_{f2} , T_{f3}), the isentropic relation-based temperature pulse

T_{isen} and the mean exhaust temperature T_m are involved to represent the extremities of temperature pulsations. The isentropic relation-based temperature T_{isen} indicates an estimation of temperature pulsation by assuming the exhaust flow is under a reversible process without viscous effect or heat transfer loss. Meanwhile, T_m measured from a 3 mm thermocouple refers to the mean value of exhaust temperature.

2.4.1. Isentropic relation-based temperature

The isentropic relation-based static temperature can be estimated using the static instantaneous pressure measurement as Mollenhauer [30]

$$T_{isen} = T_m \left(\frac{p}{p_m} \right)^{\frac{\gamma_{isen}-1}{\gamma_{isen}}} \quad (10)$$

where p_m is the mean of measured pressure of the exhaust pulse. In particular, since γ_{isen} is related to T_{isen} , the calculation of T_{isen} in Eq. (10) is an iterative procedure until the waveform of γ_{isen} converges, with the maximum difference between two iterations reaching less than 0.1%. Moreover, for the engine exhaust pre-turbine pulsation which is considered as a pulsating flow with high frequency and low viscosity (i.e., high Womersley number), the mass transfer of pulses has a phase lag with respect to the pressure gradient [31,32]. The transfer of gas temperature is dependent on the mass transfer of pulses. Consequently, T_{isen} pulse, which is derived from fast pressure signals, needs to be phase-adjusted to align with the rise in temperature pulses measured by thin-wire thermocouples.

2.4.2. Quantitative comparison of crank angle-resolved flow properties

To assess the impact of using different measured or estimated temperature pulses, this study introduces the minimum R-squared (R^2) and maximum relative difference (MRD) to quantify the temperature-induced difference in flow properties throughout the exhaust event (i.e., the engine crank angle $\theta \in [EVO, EVC]$). R^2 is the smallest R-squared value obtained by comparing the waveforms of flow properties, which indicates the least likelihood of similarity between the compared waveforms:

$$R^2 = \min_{i \in [T_{pulses}]} \left\{ 1 - \frac{\sum [y_i(\theta) - y_{ref}(\theta)]^2}{\sum [y_{ref}(\theta) - y_{ref,m}]^2} \right\} \quad (11)$$

where y_i denotes a flow property evaluated by using the i th temperature pulse. y_{ref} is the reference waveform used to evaluate the change, and the subscript m denotes the mean value of a pulse.

Meanwhile, MRD represents the largest temperature-induced difference among these pulses with respect to the engine crank angle:

$$MRD = \max_{i \in [T_{pulses}]} \frac{|y_i(\theta_i^*) - y_{ref}(\theta_i^*)|}{y_{ref}(\theta_i^*)} \quad (12)$$

Table 3
Engine test matrix.

| Test point | Load sweep | | | | Speed sweep | | | |
|-------------------------------------|------------|------|------|------|-------------|------|------|-------|
| | LS#1 | LS#2 | LS#3 | LS#4 | SS#1 | SS#2 | SS#3 | SS#4 |
| Operating condition | | | | | | | | |
| Load [Nm] | 528 | 597 | 822 | 996 | 748 | 732 | 593 | 503 |
| Speed [rpm] | 1500 | 1500 | 1500 | 1500 | 700 | 1100 | 1500 | 1900 |
| Excess air ratio [-] | 2.26 | 2.30 | 2.28 | 2.32 | 1.99 | 2.05 | 2.27 | 2.50 |
| Intake pressure [kPa abs.] | 106 | 113 | 136 | 157 | 110 | 112 | 111 | 117 |
| IMEP [kPa] | 648 | 731 | 1016 | 1203 | 805 | 862 | 745 | 696 |
| CoV of IMEP [%] | 1.95 | 1.64 | 1.57 | 1.15 | 0.86 | 1.69 | 1.47 | 3.22 |
| Single-pipe exhaust flow | | | | | | | | |
| In-cylinder trapped mass [g/cycle] | 2.31 | 2.56 | 3.32 | 3.99 | 2.69 | 2.6 | 2.54 | 2.63 |
| Fundamental frequency of pulse [Hz] | 12.5 | 12.5 | 12.5 | 12.5 | 5.83 | 9.17 | 12.5 | 15.83 |
| Backpressure [kPa abs.] | 104 | 104 | 105 | 105 | 103 | 103 | 104 | 105 |
| Cylinder pressure at EVO [kPa abs.] | 328 | 362 | 476 | 555 | 388 | 381 | 376 | 387 |
| Exhaust gas temperature [K] | 631 | 650 | 645 | 646 | 639 | 643 | 650 | 653 |

where $\theta_i^* \in [\text{EVO}, \text{EVC}]$ is the crank angle with the maximum relative difference when comparing the i th pulse to the reference pulse.

2.4.3. Sensitivity to gas temperature

A sensitivity analysis is performed to examine the impact of temperature pulsations on the mass flow measurement. Based on Eq. (4), the fraction change of mass flow caused by the temperature fraction change can be approximated by

$$\frac{\Delta \dot{m}}{\dot{m}} = \text{SF} \cdot \frac{\Delta T}{T} \quad (13)$$

where SF is the sensitivity factor, which is the normalized derivative of the mass flow with respect to temperature:

$$\text{SF} = \left(\frac{\partial \dot{m}}{\partial T} \right) / \left(\frac{\dot{m}}{T} \right) = -\frac{T}{2\gamma(\gamma-1)} \frac{d\gamma}{dT} + \frac{T \ln(p_0/p)}{2\gamma^2} \frac{(p_0/p)^{\frac{\gamma-1}{\gamma}}}{(p_0/p)^{\frac{\gamma-1}{\gamma}} - 1} \frac{d\gamma}{dT} - \frac{1}{2} \quad (14)$$

$$\frac{d\gamma}{dT} = -\frac{4T^3 a_5 + 3T^2 a_4 + 2T a_3 + a_2}{(c_p/Rg - 1)^2} \quad (15)$$

2.5. Test matrix

The intention of test matrix was to provide on-engine flow conditions for resolving various exhaust pulsation waveforms associated with the sweep of engine load and speed. The test matrix consists of eight test points, as listed in Table 3. After warming up the engine, the test points were operated in the sequence of completing the load sweep (LS) at 1500 rpm, followed by initiating the speed sweep (SS) from 700 rpm to 1900 rpm. The LS and SS test points were selected to isolate the effects of in-cylinder trapped mass and valve opening speed from an exhaust valve discharge perspective.

During the load sweep with a constant engine speed at 1500 rpm, the cylinder pressure at EVO increased as the engine load was increased from 500 Nm to 1000 Nm, while the fundamental frequency of exhaust pulses remained the same due to a consistent valve opening speed. Conversely, for SS test points, the in-cylinder trapped mass was kept at a comparable level to study the effect of varying engine speed (equivalent to changing valve opening speed) on exhaust pulse waveform. In particular, the engine control variables were manually adjusted to maintain a comparable mean exhaust gas temperature throughout the test matrix. More description on the design of experiments can be found in Venkataraman et al. [23]. Additionally, the coefficient of variation (CoV) [27] of the net indicated mean effective pressure (IMEP) is listed in Table 3 to indicate the combustion stability over the 300 successive engine cycles. The IMEP and CoV were calculated based on the pressure traces of the cylinder connected to the single-pipe system.

3. Results and discussion

3.1. Pressure and temperature pulsations

Fig. 3 displays the measured pressure and temperature pulses at LS#4. The crank angle is counted with respect to the crank angle degree after the engine power stroke's top dead center ($^\circ\text{CA ATDC}$). The dynamic pressure between stagnation and static pressures indicates the exhaust flow dynamics inside the single-pipe measurement section after EVO. In particular, the post-pulse expansion and compression waves can also be observed after 300°CA ATDC . For temperature measurement, the responses of thin-wire thermocouples (i.e., T_{f1} , T_{f2} , and T_{f3}) demonstrate that, due to increased thermal inertia, the attenuation of the thermocouples' response became more obvious as the wire diameters increased. T_{f1} was measured with the least thermal inertia and exhibited the largest peak-peak variation among the thermocouples, which can be attributed to its greater frequency response. In addition to thin-wire thermocouples, the mean exhaust temperature T_m from the 3 mm thermocouple and the isentropic relation-based temperature T_{isen} are also presented to indicate the bounds of potential pulse shape of the exhaust temperature. T_{isen} in Eq. (10) is determined by fast pressure measurement. Therefore, the waveform of T_{isen} was similar to the static pressure pulse, showing the immediate rise and fall when the exhaust pulse passed through the measurement section. Notably, as T_{f1} was at the lowest temperature level caused by heat losses both to the sensor base-stem and surroundings at around 144°CA ATDC , T_{isen} already rapidly reached its peak. This resulted in the largest difference among the temperature pulses.

3.2. Effect of varying temperature pulsations

As previously discussed, neither the attenuated temperature measurements nor the temperatures estimated based on the isentropic relation can accurately represent the true temperature pulsations of exhaust flows. Therefore, this subsection experimentally and analytically evaluates the effect of varying temperatures on mass flow measurement. First, the variations in flow properties are quantified and compared under different measured and estimated temperature pulses. Then, within the limits that pertain to exhaust flow conditions, a sensitivity analysis is performed to assess the influence of gas temperature variations.

3.2.1. Flow properties variation to measured and estimated temperature pulses

Fig. 4 presents the flow properties of the exhaust pulse at LS#4 regarding the different measured temperatures from thin-wire thermocouples, isentropic relation-based temperature, and the mean temperature from 3 mm thermocouple. The temperature-induced differences were evaluated numerically and compared based on the flow properties using fastest temperature measurement T_{f1} as the reference signal for

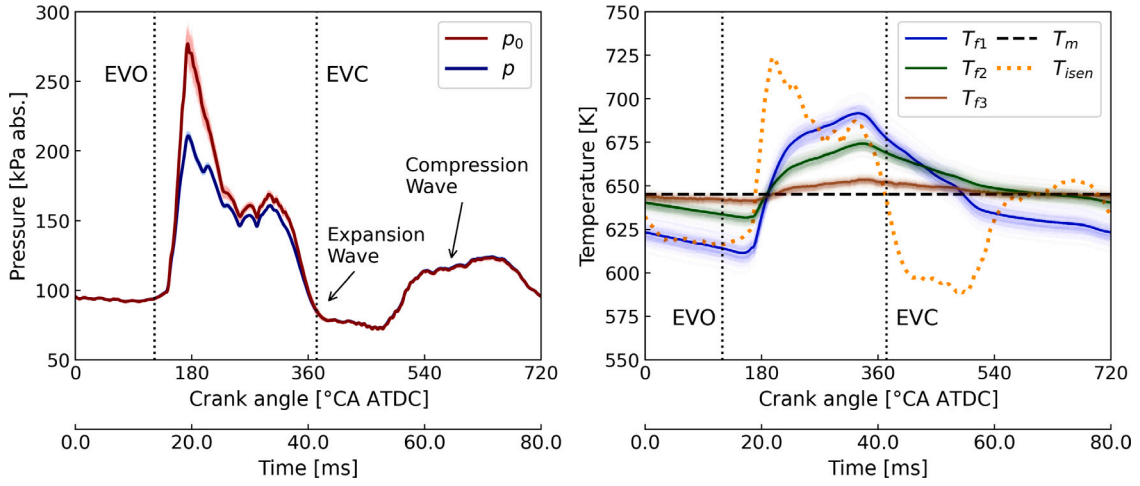


Fig. 3. Pressure and temperature of the engine exhaust pulsation at LS#4 with respect to crank angle degree and equivalent time. The solid lines are the cycle-averaged result of 300 engine cycles, while the shaded areas represent the pulse variation over cycles. Temperature pulses shown in the right plot are measured by thin-wire thermocouples (T_{f1} , T_{f2} , and T_{f3}) and 3 mm thermocouple (T_m) along with the estimated the isentropic relation-based temperature (T_{isen}).

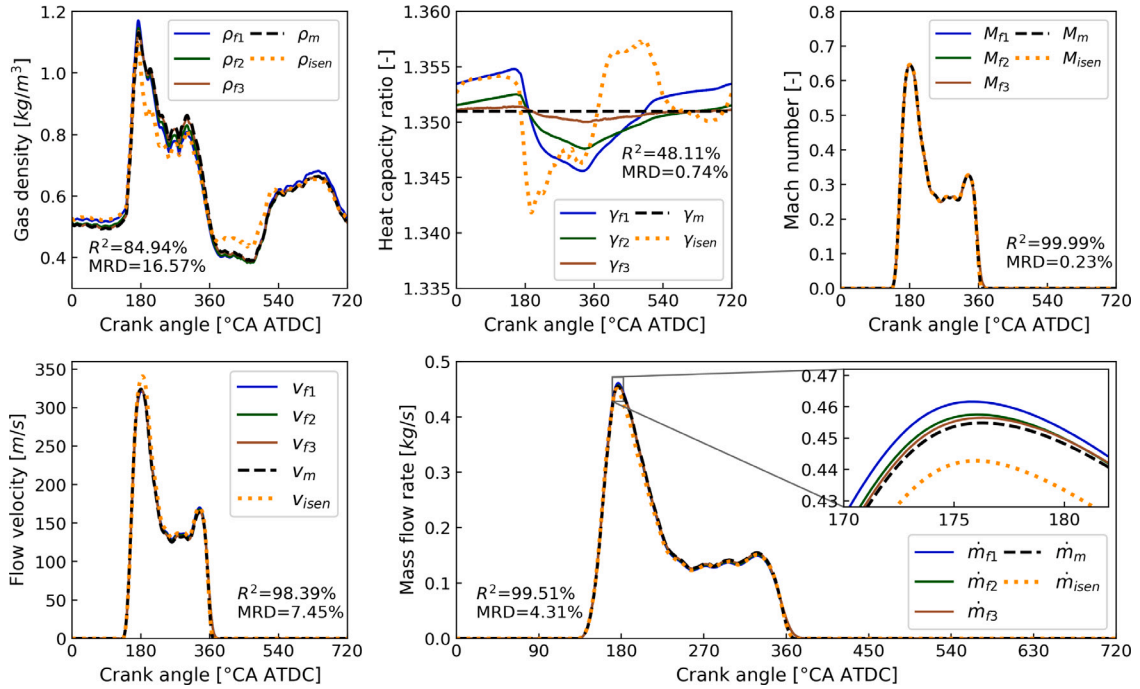


Fig. 4. Flow properties estimated using different temperature pulsations at LS#4. The subscript of notations indicates the corresponding temperature pulse.

R^2 and MRD calculations. It can be seen that the gas density waveforms estimated by different temperature pulsations were similar and the shape of the waveforms was identical to the static pressure pulse. However, in terms of the discrepancy among gas density pulses, the temperature pulsations still led to a MRD of 16.65% between ρ_{f1} and ρ_{isen} . As for the heat capacity ratio, its waveform was the inverse of temperature pulse. Therefore, although the discrepancy among the heat capacity ratio pulses was small, a significant waveform difference indicated by R^2 can still be observed. Moreover, the effect of temperature pulsation on Mach number was negligible within the measured range. The flow velocity had a similar trend as the Mach number, and only the isentropic relation-based temperature led to a noticeably higher value at the peak of the velocity pulse (i.e., the peak of v_{isen} was 7.45% higher than that of v_{f1}). Furthermore, compared to flow velocity, the mass flow under different temperature pulsations demonstrated even smaller discrepancies, with an MRD of 4.31% between \dot{m}_{f1} and \dot{m}_m observed at the peak ranges of pulses and an $R^2 \geq 99\%$ over their waveforms.

According to Eq. (4), the insignificant impact of gas temperature variation on the mass flow waveform can be interpreted as the result of inverse changes in flow velocity and gas density. At a constant pressure level, an increase in temperature results in lower gas density. However, the increased temperature leads to a higher speed of sound, indicating a higher estimated flow velocity, given that the Mach number remains unaffected by temperature changes. The opposing influence of flow velocity and gas density on mass flow measurements serves to counter-balance the impact of temperature pulsations. To quantify the mass flow sensitivity to temperature pulsations, a sensitivity analysis is conducted in the following subsection.

3.2.2. Sensitivity to gas temperature

As shown in Eq. (14), the sensitivity factor to gas temperature $SF(T, p_0/p, \lambda)$ not only relates to the gas temperature but also involves the stagnation-to-static pressure ratio and the gas composition of combustion products determined by λ . The ranges of these variables were

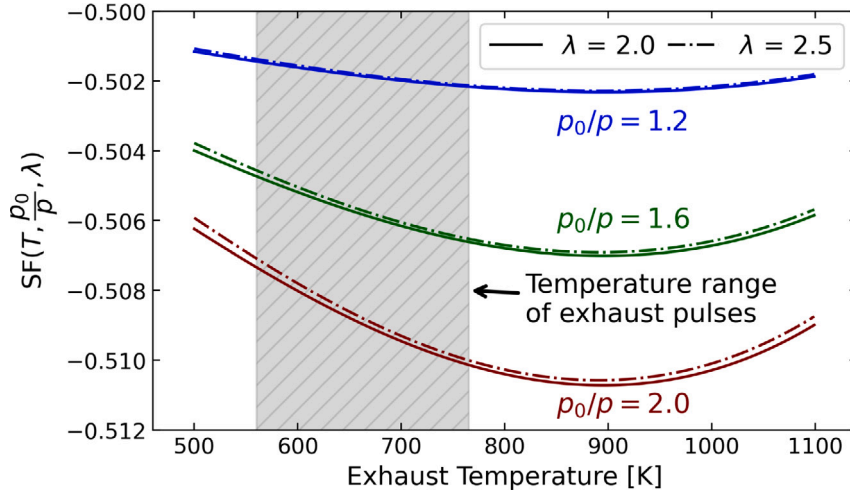


Fig. 5. Sensitivity factor of mass flow rate to gas temperature.

Table 4

The discrepancy of mass flows using different temperature pulsations. The reference signal for the R^2 and MRD calculation is m_{f1} using fast temperature from the 50.8 μm thermocouple.

| | LS#1 | LS#2 | LS#3 | LS#4 | SS#1 | SS#2 | SS#3 | SS#4 |
|-----------|-------|-------|-------|-------|-------|-------|-------|-------|
| R^2 [%] | 99.68 | 99.96 | 99.84 | 99.51 | 99.99 | 99.70 | 99.84 | 99.81 |
| MRD [%] | 3.52 | 1.63 | 4.67 | 4.31 | 3.61 | 2.72 | 2.05 | 4.18 |

set pertaining to exhaust flow conditions measured across the test matrix.

Fig. 5 depicts the sensitivity factor of mass flow concerning temperature change. The sensitivity factor ranged between -0.50 and -0.51 , indicating that the relative change in mass flow rate was approximately half of the relative change in gas temperature. The negative sensitivity factor implies that an increase in gas temperature resulted in a decrease in mass flow estimation. This observation explains the temperature-induced differences among mass flow peaks shown in Fig. 4. T_{isen} increased rapidly around 175°CA ATDC, while the temperature pulses of thin-wire thermocouples remained below the mean exhaust temperature values (see Fig. 3). Consequently, at that point, the lowest T_{f1} peak resulted in the highest m_{f1} peak. Additionally, compared to λ , the stagnation-to-static pressure ratio had a more significant influence on the sensitivity factor. However, within the limits pertaining to exhaust flow conditions, the change caused by these two variables is negligible.

The potential largest temperature-induced mass flow difference can also be evaluated based on the sensitivity factor. As the widest MRD between T_{f1} and other measured or estimated temperature pulsations across the test matrix was 9.7% (occurring at LS#4 between T_{f1} and T_{isen}), the corresponding MRD of mass flow was approximately -4.9% as determined by Eq. (13). Note that, although the effect of different temperature pulsations is not negligible, these differences only occurred at the peak of mass flow pulses, while the waveform discrepancy of mass flow pulses and the overall difference among the pulses were not significant. For operating points across the test matrix, the mass flow discrepancy caused by different temperature pulsations is listed in Table 4. Given the mass flow rate m_{f1} as the reference for R^2 and MRD calculations, it can be seen that $R^2 \geq 99\%$ for all the test points, while the MRD is less than 5%. Due to the relative insensitivity to temperature pulsations, the fast temperature measured from the 50.8 μm thin-wire thermocouple was chosen for mass flow measurements in the rest of this study.

3.3. Comparison of in-cylinder trapped mass

Fig. 6 compares in-cylinder trapped mass values obtained via the Pitot tube-based approach and the reference λ -based estimation. Aside

from a 3.4% difference in SS#1, discrepancies between the techniques were under 2% for the entire test matrix. It should be noted that the Pitot tube tip measures on the pipe centerline where the velocity profile is flatter and less influenced by wall-induced friction. However, at low exhaust mass flow rates, the trapped mass measured by the Pitot tube-based method might be lower than the reference. This is due to the sensor's accuracy in measuring stagnation and static pressure. Given a dynamic pressure measurement uncertainty of $u_{dp} \approx 1.4$ kPa (see Appendix C), test points with lower flow rates may have increased measurement uncertainty. Additionally, the experimental uncertainty of the mass flow rate measurement is estimated in Appendix D with the relative uncertainty, denoted as u_m/\dot{m} , reaching up to $\pm 2.7\%$ under the measured exhaust flow conditions.

3.4. Exhaust mass flow pulse characteristics

This subsection presents the crank angle-resolved mass flows measured by the Pitot tube-based approach. The mass flow of exhaust pulses is discussed with a focus on how the pulse behaves in terms of the blow-down phase and the scavenge phase. The blow-down and scavenge phases through the exhaust event can be described as:

- The blow-down phase begins at EVO as the high in-cylinder pressure after the combustion drives the expansion of cylinder gas into the exhaust system. Throughout the blow-down phase, the mass flow rate increases to the maximum. The pressure difference between the cylinder and the exhaust pipe progressively decreases towards equilibrium. Subsequently, the exhaust event transitions to the scavenge phase.
- During the scavenge phase, piston movement primarily drives the development of the exhaust flow. Gas-exchange processes occurring in the scavenge phase, such as pressure wave reflections within the exhaust pipe and the overlapping of intake and exhaust valve openings, also influence exhaust flow conditions.

In this subsection, the characterization of mass flow pulses across the test matrix is analyzed in terms of pulse waveforms, arrival times at the measurement section, and mass distributions through blow-down and scavenge phases. Furthermore, the relationship between cycle-to-cycle variations in mass flow pulses and relevant gas-exchange is discussed.

3.4.1. Load sweep

Fig. 7(a) displays mass flow pulses across the load sweep. The peak magnitudes of these mass flow pulses increased under the load sweep, and all the pulse peaks occurred around 175°CA ATDC. This

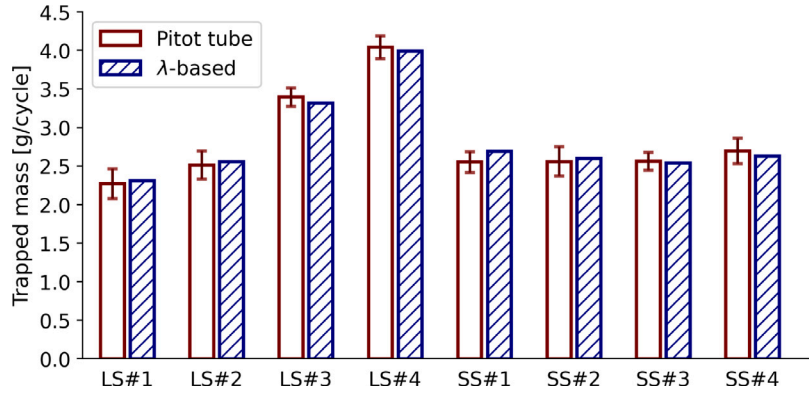


Fig. 6. Comparison of in-cylinder trapped mass. Error bars are 2σ -level deviation of trapped mass over cycles.

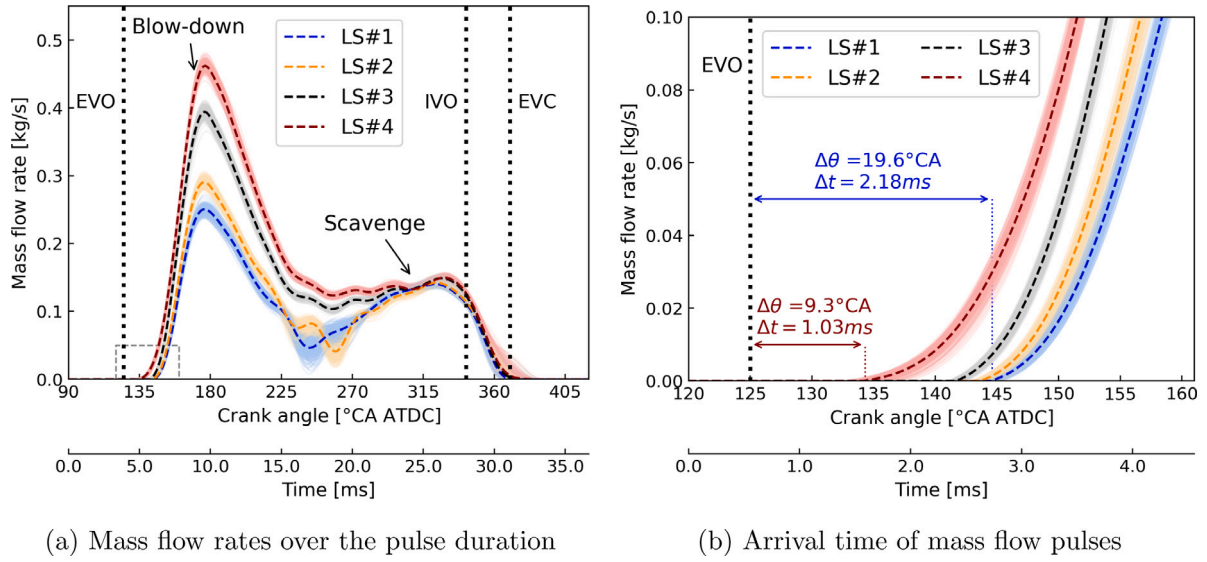


Fig. 7. Exhaust mass flow pulses under the load sweep, and the zoom-in view of the pulse arrival time at the single-pipe measurement section. The dashed line is the cycle-averaged mass flow rate of 300 cycles, while the shaded area represents the variation in mass flow pulses over cycles.

is expected because a higher EVO pressure ratio across the valve (see Table 3) resulted in greater instantaneous mass flow rates at a constant valve opening speed [33]. Moreover, despite the increase in the trapped mass with the load, the magnitude of the scavenge phase remained unchanged. In other words, the increasing trapped mass was predominantly discharged during the blow-down phase, and thus leading to a higher peak in mass flow pulsation. Additionally, the pulse duration was almost unvaried under the load sweep with comparable blow-down and scavenge phase durations throughout the load sweep. This can be attributed to the LS points having a consistent firing frequency at a constant engine speed, which in turn determines the instantaneous valve opening and closing speeds along with the piston velocity. Hence, for the LS points the timescale of engine exhaust pulses and wave action in the exhaust pipe remained consistent.

Fig. 7(b) presents the pulse arrival time at the measurement section. As the Pitot tube was located downstream of the single-pipe, the pulsating flow arrived at the measurement section with a time delay. The pulse arrival time advanced as the engine load increased. The travel time of the mass flow pulses from the exhaust valve to the measurement section reduced from 19.6°CA ATDC at LS#1 to 9.3°CA ATDC at LS#4, which indicated the flow speed at LS#4 was twice of that at LS#1. Due to the greater cylinder pressure at EVO with an increase in engine load, the exhaust static pressure pulse was advanced in phase and increased in amplitude with load. The faster and earlier pressure rise rate in the exhaust indicates a faster pressure wave propagation

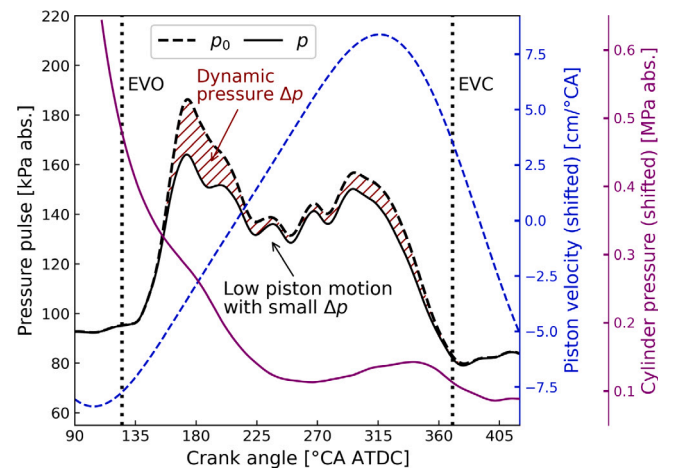


Fig. 8. Pressure pulses in the single-pipe measurement section and the in-cylinder condition at LS#1. The positive piston velocity indicates the piston's motion from BDC towards TDC.

velocity [34], which manifests as a phase advanced mass flow at the measurement section with the load increase.

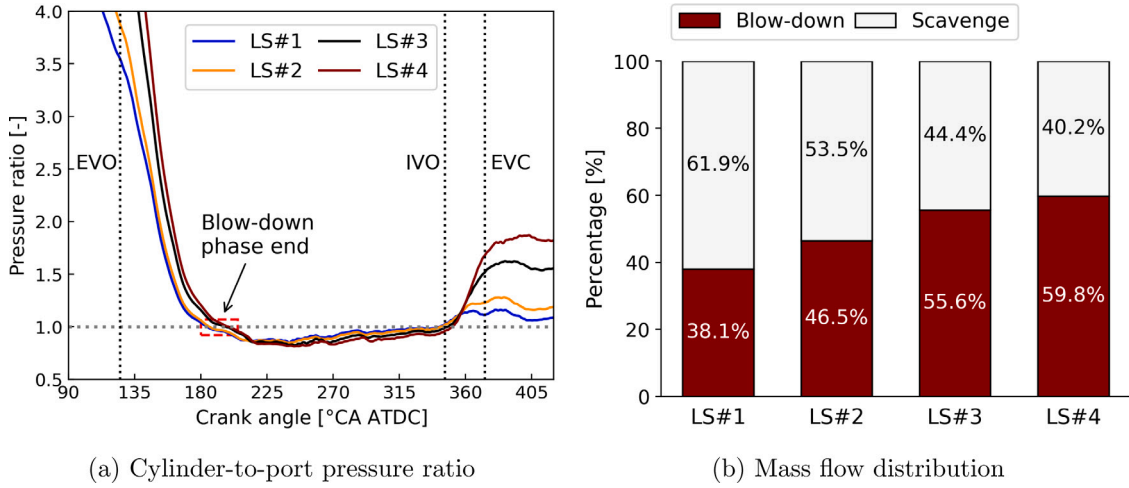


Fig. 9. Exhaust flow conditions of the blow-down and scavenge phases under the load sweep.

Fig. 8 demonstrates the relationship between the exhaust pressure pulses and the in-cylinder condition. The dynamic pressure, as the difference between stagnation and static pressure pulses, indicates the mass flow rates across the single-pipe measurement section. The in-cylinder condition, as the boundary condition of the exhaust pulse, can be discussed in terms of the cylinder pressure and piston motion (i.e., piston velocity). Note that the measurement of exhaust flow in the single-pipe system and in-cylinder condition had the time delay due to the flow propagation. Therefore, for comparison, the phases of piston velocity and cylinder pressure in Fig. 8 are shifted based on the pressure pulse arrival time at the measurement section. It can be seen that after EVO, with the continuous discharge of the cylinder gas, the cylinder pressure reduced to the equilibrium with the exhaust pipe (i.e., the end of the blow-down phase), then the rest exhaust flow was mainly developed by the piston movement (i.e., the scavenge phase). The large dynamic pressure at the beginning indicates the high mass flow rate driven by cylinder pressure. After the drop of cylinder pressure, the piston motion determined the cylinder emptying. However, the slow piston speed around BDC might cause weak flow motion, especial in cases with lower trapped mass (e.g., LS#1 and LS#2).

Fig. 9(a) presents the cylinder-to-port pressure ratio to identify the duration of blow-down and scavenge phases. It can be observed that the cylinder-to-port pressure ratio began to drop after EVO, eventually reaching equilibrium with the exhaust port pressure. The end of the blow-down phase is identified at the point when the cylinder-to-port pressure ratio equals unity. Note that, in the pursuit of equilibrium, the over-expansion of in-cylinder mass might cause the cylinder pressure to drop below port pressure, which results in the cylinder-to-port pressure ratio temporarily being less than unity during the scavenge phase. During the valve overlap between IVO and EVC, the boost pressure of intake flow increased the cylinder pressure, thereby resulting in a sharp rise in the cylinder-to-port pressure ratio. Furthermore, Fig. 9(b) presents the exhaust mass distribution through the blow-down and scavenge phases under the load sweep. As the load increased, the mass fraction of the blow-down phase increased from 38.1% of the total exhaust mass at LS#1 to 59.8% at LS#4, while the duration of the blow-down phase remained almost unchanged.

Moreover, the relationship between pulse variations over cycles (as shown in Fig. 7(a)) and gas-exchange processes can be analyzed. The cycle-to-cycle variation during the blow-down phase diminished with higher load, following the combustion CoV trend in Table 3. During the scavenge phase, the influence of gas-exchange processes was more noticeable. At low load points (LS#1 and LS#2), the variation between 225–270 °CA ATDC increased as the piston pushed residual gas at a slower speed at BDC (see Fig. 8). Due to reduced in-cylinder trapped mass and weaker blow-down at low load, exhaust pipe reflected waves

also affected cylinder discharge, resulting in more obvious pulse variation over cycles. Another exhaust period with significant pulse variation was the valve overlap between IVO and EVC. As seen in Fig. 9(a), intake pressure led to an increased in-cylinder pressure after IVO, subsequently impacting exhaust flow conditions. As a result, at high load points, the variation became larger as intake pressure increased with load.

3.4.2. Speed sweep

The speed sweep maintained consistent exhaust flow boundary conditions, only changing the pulsating flow's fundamental frequency by varying relative valve opening speeds. Fig. 10(a) reveals distinct exhaust pulse waveforms in the speed sweep when compared to the load sweep. Although the pulse duration at low-speed points appeared shorter with respect to the crank angle, their equivalent time was longer than high-speed points. This led to a longer blow-down phase for low-speed operations, expelling a larger portion of exhaust flow. At SS#1, minimal exhaust remained for the scavenge phase, causing exhaust pulse discontinuity. Early cylinder emptying at SS#1 and SS#2 resulted in misaligned mass flow peak locations during the scavenge phase, deviating from the expected timing in the load sweep. As engine speed increased, exhaust pulsation peaks in the blow-down phase rose due to quicker valve opening speeds, resulting in higher mass flow rates at given pressure ratios across the valve [33]. Scavenge phase mass flow rates also increased at high speeds, merging with the blow-down portion. In short, the consistency of blow-down and scavenge phase durations, as shown in the load sweep, does not hold for the speed sweep. As the engine speed changed, the timescale of the engine exhaust pulses shifted, altering their interaction with the wave effects in the single-pipe exhaust.

As the cylinder conditions (e.g., trapped mass and cylinder pressure at EVO) were kept at a comparable level across the speed sweep, it can be seen that the change in valve opening speed and the pulse fundamental frequency both affect the speed of exhaust flow. As shown in Fig. 10(b), the exhaust mass flow pulse at high engine speed points traveled faster in the timescale. For instance, the pulse at SS#4 arrived roughly 0.5 ms earlier than the pulse at SS#1 in the time scale, even though it was delayed by 9.6 °CA compared to SS#1 with the increased engine speed. It should be noted that this time-scaled interpretation can be misleading, as the crank angle-resolved process is scaled to time based on the engine speed and will not be representative of the physical process of valve discharge.

As depicted in Fig. 11, an earlier pressure rise at the exhaust port (i.e., the single-pipe inlet) is observed in SS#3 at the beginning of the blow-down phase. This earlier pressure rise suggests a more rapid

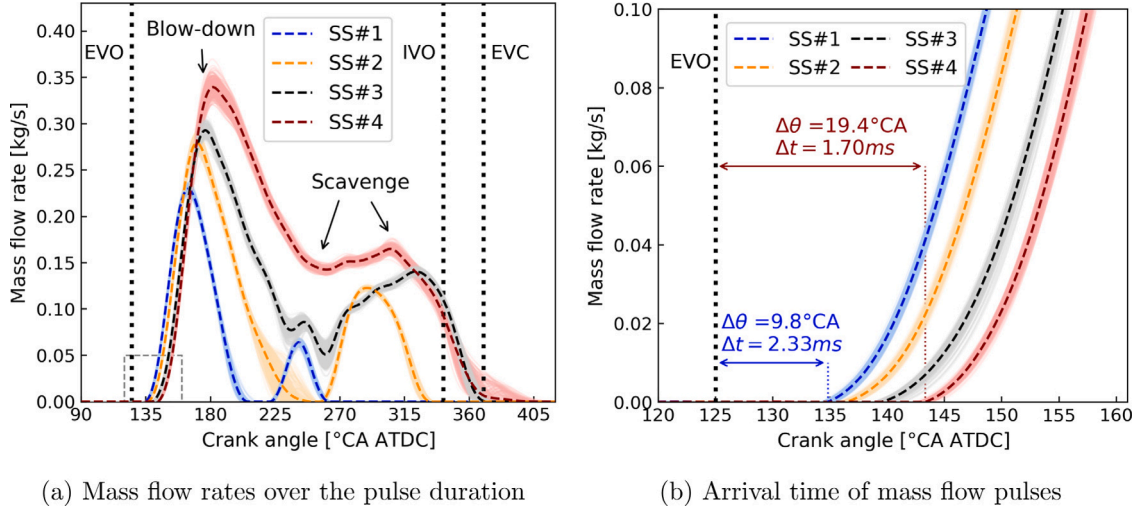


Fig. 10. Exhaust mass flow pulses under the speed sweep, and the zoom-in view of the pulse arrival time at the single-pipe measurement section. The dashed line is the cycle-averaged mass flow rate of 300 cycles, while the shaded area represents the variation in mass flow pulses over cycles.

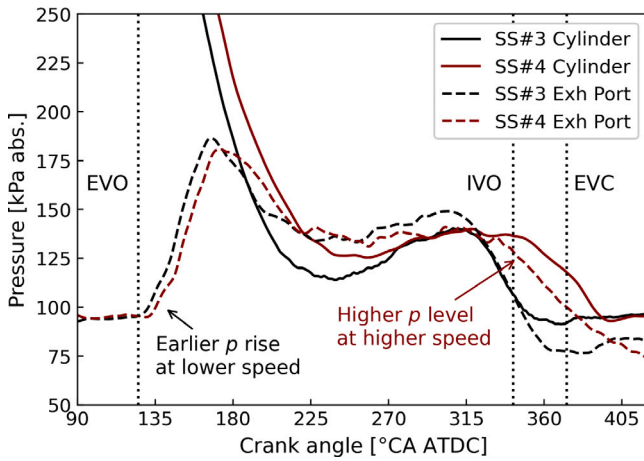


Fig. 11. Comparison of cylinder and exhaust port pressures at SS#3 and SS#4.

flow propagation in lower engine speed cases [34]. Moreover, Fig. 11 reveals that both cylinder and exhaust port pressures at SS#4 were higher than those at SS#3 when the scavenge phase was nearing its end. Since the speed sweep maintained in-cylinder trapped mass and boost pressure at comparable levels, the increased pressure was primarily due to a greater amount of exhaust gas remaining in the cylinder, resulting from the faster engine speed. This observation also implies that, with increasing speed, more in-cylinder mass remained to be expelled for the scavenge phase.

The spread of the end timing for the blow-down phase, as shown in Fig. 12(a), was larger under the speed sweep than under the load sweep. Additionally, the duration of the exhaust event increased with engine speed, prolonging the crank angle period for the blow-down phase and retarding the scavenge phase. The exhaust mass distribution in Fig. 12(b) indicates that although the pulse duration of the blow-down phase was prolonged, the mass fraction of the blow-down phase decreased as the speed increased. As the blow-down phase was considered with the most exhaust energy to produce work in the WER systems [35], the mass fraction drop of the blow-down phase indicates less exhaust energy was available in cases with faster engine speed.

Similar to the load sweep, the cycle-to-cycle pulse variation of mass flow pulses during the blow-down phase corresponded with the combustion CoV under the speed sweep. The largest variation in the blow-down phase occurred at SS#4 due to the lowest combustion stability. In terms of the pulse variation during the scavenge phase, although the low piston motion at BDC can lead to high pulse variations, the influence of low piston motion on pulse variation at SS#1 was relatively less due to its flow discontinuity. Furthermore, since the exhaust discharge at SS#1 and SS#2 was completed before IVO, there was no interaction with the valve overlap between IVO and EVC at these low-speed points. In contrast, the pulse duration at high speeds was prolonged into the valve overlap period, during which the intake flow caused noticeable pulse variations in mass flow pulses.

4. Summary and conclusions

This study contributes to characterizing the crank angle-based mass flow rate from an isolated cylinder exhaust of a HD engine using a single-pipe measurement system, developed for pulsating flow measurement. A Pitot tube technique was utilized to capture the stagnation pressure of exhaust pulses for mass flow calculation. Meanwhile, customized unsheathed thin-wire thermocouples were used for fast temperature measurement. However, due to the thermal inertia of the thermocouple junction, the fast temperature measurement used in the proposed approach might still be attenuated to some extent. Therefore, this study investigated the impact of attenuated temperature pulses on mass flow measurement.

- Based on the analytical solution derived from sensitivity analysis, a temperature-induced difference of up to 4.9% in instantaneous mass flow measurements can be attributed to the attenuation of temperature pulses. However, subsequent numerical analysis using measurement results demonstrated that such deviations primarily occur at the peak of exhaust pulses. Moreover, the overall waveform discrepancy in mass flow pulses, resulting from attenuated temperature pulses, was insignificant (i.e., $R^2 \geq 99\%$ among mass flow pulses).

According to the conclusion above, the fast temperature measurement from the 50.8 μm thermocouple was selected to resolve mass flow pulses in the Pitot tube-based approach. The in-cylinder trapped

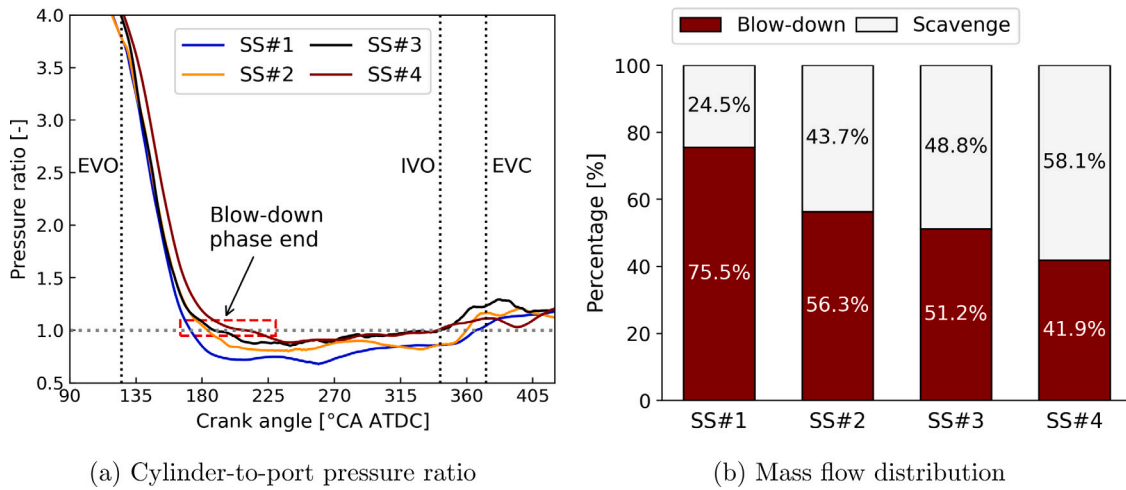


Fig. 12. Exhaust flow conditions of the blow-down and scavenge phases under the speed sweep.

mass calculated using both the Pitot tube and the λ -based estimation methods were then compared to evaluate the accuracy and consistency of the Pitot tube-based approach.

- Except of the lowest engine speed point (SS#1), the in-cylinder trapped mass discrepancy between the results of the Pitot tube approach and the λ -based estimation remained below 2% across the test matrix. While, a trapped mass discrepancy of 3.4% at SS#1 was caused by the accuracy limit of fast pressure transducers.

The test matrix, involving sweeps of engine load and speed, was specifically designed to isolate the effects of valve opening speed and in-cylinder trapped mass. The mass flow waveforms of exhaust pulsations were analyzed regarding the change in pulse shapes during the blow-down phase and the subsequent scavenge phase. Furthermore, this study also discusses the arrival time of pulses at the measurement section, the mass distribution throughout two exhaust phases, and the variation in mass flow pulses over cycles.

- For the load sweep, the pulse duration of both the blow-down and scavenge phases remained relatively unchanged due to the constant engine speed. The main change in mass flow waveform occurred during the blow-down phase, as pulse peak magnitudes increased with load, and the timings of pulse peaks consistently appeared around 175 °CA ATDC. In contrast, the scavenge phase's pulse peak and waveform were unaffected. The mass fraction of the blow-down phase increased with engine load, from 38.1% at LS#1 to 59.8% at LS#4. Furthermore, due to the higher cylinder pressure at EVO, an earlier arrival time of exhaust pulses was observed in cases with a higher load.
- The waveform of mass flow pulses varied significantly under the speed sweep. The pulse magnitude and duration of the blow-down phase increased with engine speed. The arrival time (in crank angle domain) of the exhaust pulse was delayed at high-speed cases. The blow-down and scavenge parts of the exhaust pulse were temporally separated at low speed and merged together as the engine sped up. Consequently, the mass fraction of the blow-down phase decreased from 75.5% at SS#1 to 41.9% at SS#4. This reduction in blow-down mass flow indicated a diminished work potential in the exhaust pulses for WER, considering the blow-down phase is defined as the period with the most available exhaust energy in literature.
- The variation in mass flow pulses over cycles corresponded closely with combustion stability during the blow-down phase. However, through the scavenge phase, this variation was primarily influenced by gas-exchange processes. For instance, the valve overlap between IVC and EVO impacted the exhaust flow variation as the boost pressure interacted with the expulsion of exhaust gases.

5. Nomenclature

| | |
|-----------|----------------------------------|
| p | Pressure [kPa abs.] |
| T | Temperature [K] |
| \dot{m} | Mass flow rate [kg/s] |
| θ | Crank angle [°CA] |
| ρ | Gas density [kg/m ³] |
| λ | Excess air ratio [–] |
| ω | Engine speed [rpm] |
| γ | Ratio of heat capacity [–] |
| c_p | Heat capacity [kJ/K] |
| M | Mach number [°CA] |
| c | Speed of sound [m/s] |
| v | Flow velocity [m/s] |
| u | Measurement uncertainty [–] |

Subscripts

| | |
|-----------|--------------------------------------|
| 0 | Stagnation |
| $f1$ | 50.8 μ m thermocouple |
| $f2$ | 76.2 μ m thermocouple |
| $f3$ | 254 μ m thermocouple |
| m | Mean value of a pulse |
| $isen$ | Isentropic relation-based estimation |
| $trapped$ | Trapped mass per cylinder |

Acronyms

| | |
|-----------|---|
| ICE | Internal combustion engine |
| HD | Heavy-duty |
| WER | Waste energy recovery |
| MIMS | Conventional mineral insulated metal sheathed |
| PIV | Particle image velocimetry |
| PSD | Power spectral density |
| VGT | Variable geometry turbocharger |
| IVO (IVC) | Intake valve opening (closing) |
| EVO (EVC) | Exhaust valve opening (closing) |
| LS | Load sweep |
| SS | Speed sweep |
| IMEP | Indicated mean effective pressure |
| CoV | Coefficient of variation |
| AFR | Air-fuel ratio |
| FS | Full scale |
| (A)TDC | (After) top dead center |
| BDC | Bottom dead center |
| MRD | Maximum relative difference |

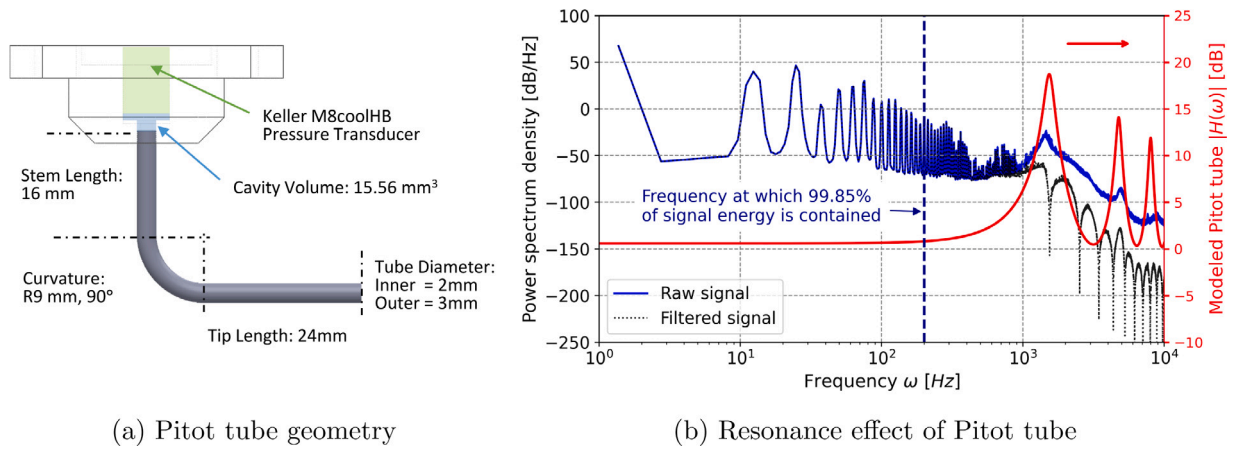


Fig. A.13. Pitot tube geometry and its resonance effect on stagnation pressure measurement.

Declaration of competing interest

The authors declare that they have no known competing financial interests or personal relationships that could have appeared to influence the work reported in this paper.

Data availability

Data will be made available on request.

Acknowledgments

The Swedish Energy Agency (Energimyndigheten), Sweden, the Competence Center for Gas Exchange (CCGEx), Sweden and its partners are acknowledged for funding this study. The authors would like to thank Ted Holmberg for the measurement section design and experimental setup. The authors also greatly appreciate the support of Tomas Östberg at KTH Royal Institute of Technology in Pitot tube machining and test rig setup. The insightful discussion with Yushi Murai at KTH Fluid Physics Laboratory is particularly acknowledged.

Appendix A. Pitot tube geometry and its resonance effect

Fig. A.13 presents the designed Pitot tube geometry and the associated resonance effect. The resonance effect on stagnation pressure measurement is exemplified when the engine operates at LS#2 with 597 Nm and 1500 rpm. The Pitot tube is made of stainless steel with the geometry shown in Fig. A.13(a). To thermally isolate the fast pressure transducer from the exhaust temperature, the pressure transducer was mounted on the Pitot tube with its cooling system. The channel volume from the Pitot tube tip to the pressure transducer location forms an acoustic system. The design of the Pitot tube needs to take its resonance frequency into account to avoid interaction with the natural frequency of the exhaust pulses. The transfer function of the Pitot tube's resonance behavior was modeled as a pneumatic line-cavity system [36].

Fig. A.13(b) displays the resonance effect by presenting the measured power spectral density (PSD) of the stagnation pressure signal. The PSD is computed using Welch's overlapped segment averaging estimator [37]. The modeled and measured resonances matched well, particularly with regard to the peaks at resonant frequency. Furthermore, the resonance effect of the designed Pitot tube was kept within the high-frequency range, ensuring that 99.85% of the signal energy spectrum remained unaffected. Additionally, high-frequency noise (i.e., elevated PSD of the raw signal) within the resonance frequency range is eliminated by employing a second-order zero-phase shift Savitzky–Golay filter [38] with a window size of 101 samples. The PSD comparison between the raw and filtered signals reveals that the selected filter effectively attenuated the resonances without impacting the signal at frequencies preceding the first resonance peak.

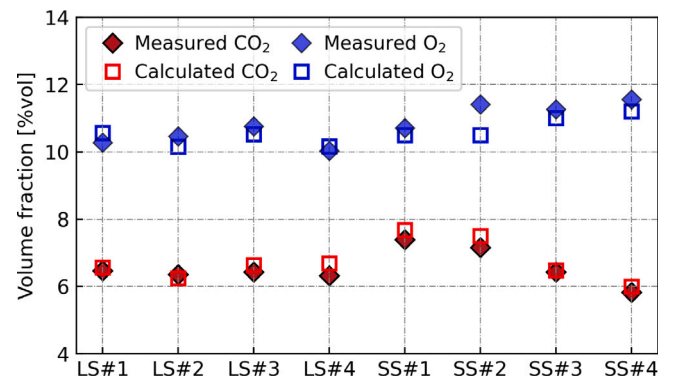


Fig. B.14. Measured and calculated CO₂ and O₂ in the single-pipe measurement system.

Appendix B. Exhaust gas composition comparison

The thermochemical properties of diesel exhaust flow are determined by the gas composition, which primarily consists of carbon dioxide and evaporated water (as products of complete combustion), as well as the oxygen and nitrogen from the remaining air after combustion. As the measurements of exhaust gas concentrations of nitrogen and evaporated water are not included in the emission analyzer, the volume fraction of exhaust gas composition is computed by the combustion chemical reaction based on the air-fuel ratio. The combustion process in this simulation is assumed to be complete combustion, while the measured carbon monoxide (CO) and hydrocarbon (HC) emissions are used to slightly adjust air-fuel ratios across the test matrix.

A detailed multi-component chemical kinetic mechanism from Lawrence Livermore National Laboratory [39] is selected in this work for the combustion simulation, and the mixture of 77% of n-dodecane (n-C₁₂H₂₆) and 23% of m-xylene (n-C₈H₁₀) is used as a diesel fuel surrogate. Fig. B.14 presents the comparison of measured and calculated CO₂ and O₂ from the exhaust flow in the single-pipe measurement system. The measured O₂ is derived from the λ measurement in the Horiba gas analyzer based on the oxygen balance.

Appendix C. Measurement uncertainty for dynamic pressure

The Pitot tube-based approach is based on the dynamic pressure, which is the difference between the measured stagnation and static pressures (see Eq. (2)). As the sensor accuracy of stagnation and static pressure transducers employed was $\pm 0.1\%$ with 1 MPa full scale, the uncertainty of measuring stagnation and static pressures in this

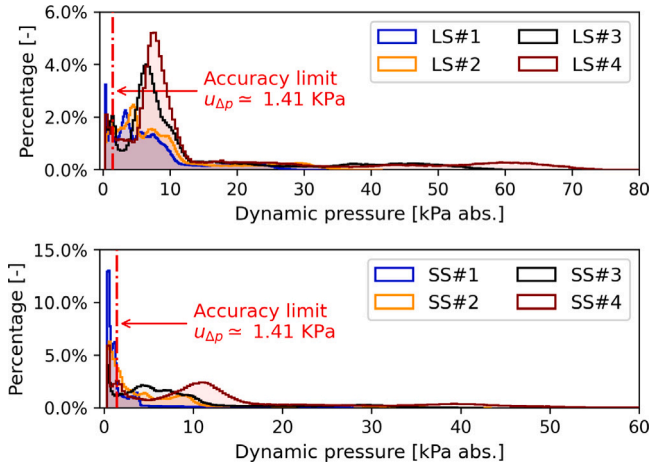


Fig. C.15. The distribution of non-zero dynamic pressure through the exhaust event for the load sweep (top) and the speed sweep (bottom).

study was taken as 1 kPa. Therefore, uncertainty of dynamic pressure measurement $u_{\Delta p}$ can be evaluated by using measurement chain as

$$u_{\Delta p} = \sqrt{\left(\frac{\partial \Delta p}{\partial p_0} u_{p_0}\right)^2 + \left(\frac{\partial \Delta p}{\partial p} u_p\right)^2} \approx 1.4 \text{ kPa} \quad (\text{C.1})$$

The distribution of non-zero dynamic pressure during the exhaust event is depicted in Fig. C.15. It can be observed that dynamic pressure in the case with lower flow rates exhibits a more extensive distribution below the threshold of 1.4 kPa, at which the sensor uncertainty limits the mass flow measurement. In particular, the mass flow measurement at SS#1 is likely to be subject to increased error, given that its dynamic pressure is predominantly distributed within the range smaller than the uncertainty limit.

Appendix D. Experimental uncertainty of mass flow rate measurement

The present work attempts to perform accurate mass flow rate measurements in pulsating exhaust flows. The experimental uncertainty in the Pitot tube-based approach involves a long measurement chain, which begins with sensor calibrations and extends to the derivation of the instantaneous mass flux based on Mach number and temperature pulses. The aim of this section is to assess the experimental uncertainties associated with the measurement techniques listed in Table 2. To eliminate the measurement drift, sensors and devices employed in the experimental campaign have been zero- and span-calibrated. Note that the upper limit for static calibration of thermocouples is up to 350 °C. Further information regarding sensor calibration is available in Venkataraman et al. [23].

The analysis firstly evaluates the uncertainty induced by emission measurement errors in the Horiba gas analyzer. Calculations using the Cantera Python library show that the $\pm 1\%$ FS measurement errors in exhaust gas composition at each selected operating point lead to a variation of less than $\pm 0.01\%$ in the heat capacity ratio within the temperature range of 500 K to 800 K. Consequently, it concludes that the uncertainty in emission readings from the Horiba gas analyzer does not influence the heat capacity ratio calculation, as this calculation depends only on temperature measurements.

The mass flow rate in the proposed Pitot tube-based approach can be expressed as a function of stagnation and static pressures, as well as the gas temperature, denoted as $\dot{m}(p_0, p, T)$. The experimental uncertainty for this approach can be estimated by the error propagation formula [40] as follows:

$$u_{\dot{m}} = \sqrt{\left(\frac{\partial \dot{m}}{\partial p_0} u_{p_0}\right)^2 + \left(\frac{\partial \dot{m}}{\partial p} u_p\right)^2 + \left(\frac{\partial \dot{m}}{\partial T} u_T\right)^2} \quad (\text{D.1})$$

The partial derivatives of the mass flow rate can be formulated as a composite function of Mach number using the chain rule:

$$\frac{\partial \dot{m}(p_0, p, T)}{\partial p_0} = \frac{\partial \dot{m}}{\partial M} \frac{\partial M}{\partial p_0} = A \sqrt{\frac{\gamma}{RgT}} \frac{(p_0/p)^{-\frac{1}{\gamma}}}{\gamma M} \quad (\text{D.2})$$

$$\frac{\partial \dot{m}(p_0, p, T)}{\partial p} = \frac{\partial \dot{m}}{\partial M} \frac{\partial M}{\partial p} = -A \sqrt{\frac{\gamma}{RgT}} \frac{(p_0/p)^{1-\frac{1}{\gamma}}}{\gamma M} \quad (\text{D.3})$$

$$\frac{\partial \dot{m}(p_0, p, T)}{\partial T} = \frac{Ap}{T} \sqrt{\frac{T}{\gamma Rg}} \left(\gamma \frac{\partial M}{\partial \gamma} \frac{d\gamma}{dT} + \frac{M}{2} \frac{d\gamma}{dT} - \frac{\gamma M}{2T} \right) \quad (\text{D.4})$$

where the derivative of the heat capacity ratio to temperature is formulated in Eq. (15). Meanwhile, the partial derivatives of Mach number with respect to heat capacity ratio can be deduced from the isentropic relationship of compressible flow given in Eq. (1).

$$\frac{\partial M}{\partial \gamma} = \frac{M}{2} \left(\gamma^2 \log \frac{p_0}{p} - \frac{1}{\gamma - 1} \right) \quad (\text{D.5})$$

The experimental uncertainties of the pressure transducers and thermocouples are sourced from the accuracy of measurement devices and sensors listed in Table 2. The uncertainty in fast pressure and temperature measurements is taken to be 1 kPa and 0.4 K, respectively. The uncertainty of the derived mass flow rate is calculated based on the specified ranges of flow parameters pertaining to the measured exhaust flow conditions. The stagnation and static pressures in this calculation vary between 1 bar absolute and 3 bar absolute, with the constraint of maintaining $M < 1$. Meanwhile, the specified temperature range is from 500 K to 800 K. As a result, the relative uncertainty of mass flow rate measurement in the Pitot tube-based approach, denoted as $u_{\dot{m}}/\dot{m}$, ranges from $\pm 0.15\%$ to $\pm 2.37\%$. The relative uncertainty increases when the difference between the stagnation and static pressures narrows. This aligns with the uncertainty limit of dynamic pressure summarized in Appendix C. It should be noted that the experimental uncertainty analysis in this section focuses on stochastic errors. While, the total uncertainty combines systematic and stochastic errors, typically treated separately [40]. The effect of temperature pulse measurement attenuation, as a potential systematic error, has been discussed in Section 3.2.

References

- [1] International Energy Agency, CO2 emissions in 2022, transport, IEA, Paris, 2023, <https://www.iea.org/reports/co2-emissions-in-2022>. (Accessed 17 May 2023).
- [2] N. Duarte Souza Alvarenga Santos, V. Rückert Roso, A.C. Teixeira Malaquias, J.G. Coelho Baêta, Internal combustion engines and biofuels: Examining why this robust combination should not be ignored for future sustainable transportation, *Renew. Sustain. Energy Rev.* 148 (2021) 111292, <http://dx.doi.org/10.1016/j.rser.2021.111292>.
- [3] B. Al-Hanahi, I. Ahmad, D. Habibi, M.A.S. Masoum, Charging infrastructure for commercial electric vehicles: Challenges and future works, *IEEE Access* 9 (2021) 121476–121492, <http://dx.doi.org/10.1109/ACCESS.2021.3108817>.
- [4] D. Smith, B. Ozpineci, R.L. Graves, P.T. Jones, J. Lustbader, K. Kelly, K. Walkowicz, A. Birky, G. Payne, C. Sigler, J. Mosbacher, Medium- and heavy-duty vehicle electrification: An assessment of technology and knowledge gaps, 2020, <http://dx.doi.org/10.2172/1615213>, URL <https://www.osti.gov/biblio/1615213>.
- [5] B. Johnson, C. Edwards, Exploring the pathway to high efficiency IC engines through exergy analysis of heat transfer reduction, *SAE Int. J. Engines* 6 (1) (2013) 150–166, <http://dx.doi.org/10.4271/2013-01-0278>.
- [6] B. Hong, S.K. Mahendar, J. Hyvönen, A. Cronhjort, A.C. Erlandsson, Quantification of losses and irreversibilities in a marine engine for gas and diesel fuelled operation using an exergy analysis approach, in: *ASME 2000 Internal Combustion Engine Division Fall Technical Conference*, American Society of Mechanical Engineers Digital Collection, 2020, <http://dx.doi.org/10.1115/ICEF2020-2956>.
- [7] R.D. Reitz, H. Ogawa, R. Payri, T. Fansler, S. Kokjohn, Y. Moriyoshi, A. Agarwal, D. Arcoumanis, D. Assanis, C. Bae, K. Boulouchos, M. Canakci, S. Curran, I. Denbratt, M. Gavaises, M. Guenther, C. Hasse, Z. Huang, T. Ishiyama, B. Johansson, T. Johnson, G. Kalghatgi, M. Koike, S. Kong, A. Leipertz, P. Miles, R. Novella, A. Onorati, M. Richter, S. Shuai, D. Siebers, W. Su, M. Trujillo, N. Uchida, B.M. Vaglieco, R. Wagner, H. Zhao, *IJER editorial: The future of the internal combustion engine*, *Int. J. Engine Res.* 21 (1) (2020) 3–10, <http://dx.doi.org/10.1177/1468087419877990>.

- [8] Z. Liu, C. Copeland, New method for mapping radial turbines exposed to pulsating flows, *Energy* 162 (2018) 1205–1222, <http://dx.doi.org/10.1016/j.energy.2018.08.107>.
- [9] R. Mosca, M. Mihaescu, Assessment of the unsteady performance of a turbocharger radial turbine under pulsating flow conditions: Parametric study and modeling, *Energy Convers. Manage.* X 15 (2022) 100268, <http://dx.doi.org/10.1016/j.ecmx.2022.100268>.
- [10] M. Simonetti, C. Caillol, P. Higelin, C. Dumand, E. Revol, Experimental investigation and 1D analytical approach on convective heat transfers in engine exhaust-type turbulent pulsating flows, *Appl. Therm. Eng.* 165 (2020) 114548, <http://dx.doi.org/10.1016/j.applthermaleng.2019.114548>.
- [11] A. Nour Eddine, D. Chalet, X. Faure, L. Aixala, P. Chessé, Effect of engine exhaust gas pulsations on the performance of a thermoelectric generator for wasted heat recovery: An experimental and analytical investigation, *Energy* 162 (2018) 715–727, <http://dx.doi.org/10.1016/j.energy.2018.08.065>.
- [12] S. Gundmalm, A. Cronhjort, H.-E. Angstrom, Divided exhaust period: Effects of changing the relation between intake, blow-down and Scavenging Valve Area, *SAE Int. J. Engines* 6 (2) (2013) 739–750, <http://dx.doi.org/10.4271/2013-01-0578>.
- [13] H. Mahabadi pour, S.R. Krishnan, K.K. Srinivasan, Investigation of exhaust flow and exergy fluctuations in a diesel engine, *Appl. Therm. Eng.* 147 (2019) 856–865, <http://dx.doi.org/10.1016/j.applthermaleng.2018.10.109>.
- [14] B. Hong, V. Venkataraman, A. Cronhjort, Numerical analysis of engine exhaust flow parameters for resolving pre-turbine pulsating flow enthalpy and exergy, *Energies* 14 (19) (2021) <http://dx.doi.org/10.3390/en14196183>.
- [15] C. Tropea, A.L. Yarin, J.F. Foss, *Springer Handbook of Experimental Fluid Mechanics*, Springer Berlin Heidelberg, Berlin, Heidelberg, 2007, pp. 215–471, <http://dx.doi.org/10.1007/978-3-540-30299-5>.
- [16] F. Laurantzon, Flow measurements related to gas exchange applications (Ph.D. thesis), in: Trita-MEK, (2012:08) KTH Royal Institute of Technology, Fluid Physics, Competence Center for Gas Exchange (CCGE), 2012.
- [17] P. Lakshminarayanan, P. Janakiraman, M.G. Babu, B. Murthy, Measurement of pulsating temperature and velocity in an internal combustion engine using an ultrasonic flowmeter, *J. Physics E: Scientific Instruments* 12 (11) (1979) 1053.
- [18] D.A. Ehrlich, P.B. Lawless, S. Fleeter, Particle image velocimetry characterization of a turbocharger turbine inlet flow, in: International Congress & Exposition, SAE International, 1997, <http://dx.doi.org/10.4271/970343>.
- [19] D.A. Ehrlich, Characterization of Unsteady On-Engine Turbocharger Turbine Performance (Ph.D. thesis), Purdue University, 1998.
- [20] H. Nakamura, I. Asano, M. Adachi, J. Senda, Analysis of pulsating flow measurement of engine exhaust by a pitot tube flowmeter, *Int. J. Engine Res.* 6 (1) (2005) 85–93, <http://dx.doi.org/10.1243/146808705X7329>.
- [21] N. Fonseca González, J. Casanova Kindelán, J.M. López Martíñez, Methodology for instantaneous average exhaust gas mass flow rate measurement, *Flow Meas. Instrum.* 49 (2016) 52–62, <http://dx.doi.org/10.1016/j.flowmeasinst.2016.04.007>.
- [22] T.L. Bergman, A.S. Lavine, F.P. Incropera, D.P. Dewitt, *Introduction to Heat Transfer*, John Wiley & Sons, 2011.
- [23] V. Venkataraman, O. Stenlås, A. Cronhjort, Thin-wire thermocouple design for exhaust gas temperature pulse measurements in internal combustion engines, *SAE Int. J. Engines* 16 (7) (2023) <http://dx.doi.org/10.4271/03-16-07-0055>.
- [24] J.D. Anderson, *Modern Compressible Flow*, McGraw-Hill Education, 2003.
- [25] D.G. Goodwin, R.L. Speth, H.K. Moffat, B.W. Weber, Cantera: An object-oriented software toolkit for chemical kinetics, thermodynamics, and transport processes (2.5.1), 2021.
- [26] W.M. Silvis, An algorithm for calculating the air/fuel ratio from exhaust emissions, in: International Congress & Exposition, SAE International, 1997, <http://dx.doi.org/10.4271/970514>.
- [27] J.B. Heywood, *Internal Combustion Engine Fundamentals*, in: McGraw-Hill series in mechanical engineering, McGraw-Hill, New York, 1988.
- [28] G. Arwatz, C. Bahri, A.J. Smits, M. Hultmark, Dynamic calibration and modeling of a cold wire for temperature measurement, *Meas. Sci. Technol.* 24 (12) (2013) 125301, <http://dx.doi.org/10.1088/0957-0233/24/12/125301>.
- [29] G. Paniagua, R. Dénos, M. Oropesa, Thermocouple probes for accurate temperature measurements in short duration facilities, in: Turbo Expo: Power for Land, Sea, and Air, Volume 2: Turbo Expo 2002, Parts A and B, American Society of Mechanical Engineers Digital Collection, 2002, pp. 209–217, <http://dx.doi.org/10.1115/GT2002-30043>.
- [30] K. Mollenhauer, Measurement of instantaneous gas temperatures for determination of the exhaust gas energy of a supercharged diesel engine, in: National Fuels and Lubricants, Powerplants, Transportation Meetings, SAE International, 1967, <http://dx.doi.org/10.4271/670929>.
- [31] J.E. Dec, J.O. Keller, I. Hongo, Time-resolved velocities and turbulence in the oscillating flow of a pulse combustor tail pipe, *Combust. Flame* 83 (3) (1991) 271–292, [http://dx.doi.org/10.1016/0010-2180\(91\)90075-M](http://dx.doi.org/10.1016/0010-2180(91)90075-M).
- [32] F. Hellström, Numerical computations of the unsteady flow in turbochargers (Ph.D. thesis), KTH, 2010.
- [33] P. Winroth, C.L. Ford, P.-H. Alfredsson, On discharge from poppet valves: effects of pressure and system dynamics, *Exp. Fluids* 59 (2) (2018) 1–15, <http://dx.doi.org/10.1007/s00348-017-2478-8>.
- [34] W.J.D. Annand, G.E. Roe, *Gas Flow in the Internal Combustion Engine: Power, Performance, Emission Control, and Silencing*, GT Foulis, 1974.
- [35] H. Mahabadi pour, K.K. Srinivasan, S.R. Krishnan, S.N. Subramanian, Crank angle-resolved exergy analysis of exhaust flows in a diesel engine from the perspective of exhaust waste energy recovery, *Appl. Energy* 216 (2018) 31–44, <http://dx.doi.org/10.1016/j.apenergy.2018.02.037>.
- [36] H. Bergh, H. Tjeldeman, Theoretical and Experimental Results for the Dynamic Response of Pressure Measuring Systems, Technical Report, National Aeronautical and Astronautical Research Institute, Amsterdam, 1965.
- [37] P. Welch, The use of fast Fourier transform for the estimation of power spectra: A method based on time averaging over short, modified periodograms, *IEEE Trans. Audio Electroacoust.* 15 (2) (1967) 70–73, <http://dx.doi.org/10.1109/TAU.1967.1161901>.
- [38] R.W. Schafer, What is a savitzky-golay filter? [lecture notes], *IEEE Signal Process. Mag.* 28 (4) (2011) 111–117, <http://dx.doi.org/10.1109/MSP.2011.941097>.
- [39] Y. Pei, M. Mehl, W. Liu, T. Lu, W.J. Pitz, S. Som, A multicomponent blend as a diesel fuel surrogate for compression ignition engine applications, *J. Eng. Gas Turbines Power* 137 (11) (2015) <http://dx.doi.org/10.1115/1.4030416>, 111502.
- [40] H. Coleman, W. Steele, *Experimentation, Validation, and Uncertainty Analysis for Engineers*, Wiley, 2018.